

Supplementary Materials

Xiangming Xue, Vidisha Ganesh, Ashwin Iyer, Daniel Roque, Xiaoning Jiang *Fellow, IEEE*, and Nitin Sharma
Senior Member, IEEE

S1. KOOPMAN OPERATOR AND LINEAR PREDICTORS

Koopman operator theory enables a nonlinear dynamical system to be represented as a linear process in a higher-dimensional space of observables [1]. Consider the discrete-time, control-affine form of the tremor system:

$$x_{k+1} = f(x_k, u_k), \quad (1)$$

where $x_k \in \mathbb{R}^n$ is the state (e.g., wrist kinematics), $u_k \in \mathbb{R}^m$ is the control or input (e.g., ultrasound-derived muscle displacement features), and f is an unknown nonlinear map.

Let $\Psi : \mathbb{R}^n \times \mathbb{R}^m \rightarrow \mathbb{R}^{N_K}$ be a vector of observables containing the original states, a set of n_ψ user-defined nonlinear basis functions $\phi(x_k)$, and the inputs:

$$\Psi_k^\top = [x_k^\top \quad \phi(x_k)^\top \quad u_k^\top], \quad N_K = n + n_\psi + m. \quad (2)$$

The Koopman operator \mathcal{K} advances these observables forward one step:

$$\mathcal{K}\Psi(x_k, u_k) = \Psi(x_{k+1}, u_{k+1}), \quad (3)$$

where $u_{k+1} = h(x_k, u_k)$ describes input evolution. In practice, \mathcal{K} is infinite-dimensional but is approximated by a finite matrix $K \in \mathbb{R}^{N_K \times N_K}$.

The lifted state Ψ_k then evolves as:

$$\Psi_{k+1} \approx K\Psi_k. \quad (4)$$

Partitioning K according to states, lifted coordinates, and inputs gives:

$$\begin{bmatrix} x_{k+1} \\ \phi(x_{k+1}) \\ u_{k+1} \end{bmatrix} \approx \begin{bmatrix} A_{11} & A_{12} & B_{11} \\ A_{21} & A_{22} & B_{21} \\ * & * & * \end{bmatrix} \begin{bmatrix} x_k \\ \phi(x_k) \\ u_k \end{bmatrix}. \quad (5)$$

The top two block rows define the finite-dimensional linear predictor:

$$z_{k+1} = Az_k + Bu_k, \quad (6)$$

where $z_k = [x_k^\top, \phi(x_k)^\top]^\top$, $A = \begin{bmatrix} A_{11} & A_{12} \\ A_{21} & A_{22} \end{bmatrix}$, and $B = \begin{bmatrix} B_{11} \\ B_{21} \end{bmatrix}$.

To estimate A and B from M data snapshots, define:

$$\begin{aligned} X &= [x_1 \quad \cdots \quad x_M], \\ X^+ &= [x_1^+ \quad \cdots \quad x_M^+], \\ U &= [u_1 \quad \cdots \quad u_M], \end{aligned} \quad (7)$$

where $x_k^+ = f(x_k, u_k)$. Applying $\Psi(\cdot)$ gives:

$$\begin{aligned} X_{\text{lift}} &= [\Psi(x_1, u_1) \quad \cdots \quad \Psi(x_M, u_M)], \\ X_{\text{lift}}^+ &= [\Psi(x_1^+, u_1^+) \quad \cdots \quad \Psi(x_M^+, u_M^+)]. \end{aligned} \quad (8)$$

The Koopman approximation is obtained from the least-squares problem:

$$K = \arg \min_{\tilde{K}} \|X_{\text{lift}}^+ - \tilde{K}X_{\text{lift}}\|_F^2. \quad (9)$$

For $M \gg N_K$, the equivalent normal-equation form is:

$$K = X_{\text{lift}}^+ X_{\text{lift}}^\top (X_{\text{lift}} X_{\text{lift}}^\top)^\dagger, \quad (10)$$

where $(\cdot)^\dagger$ denotes the Moore–Penrose pseudoinverse. Finally, A and B are extracted from K via (5). For further details, see [2]–[6]. This yields a linear, interpretable model in the lifted coordinates that captures nonlinear tremor dynamics while remaining suitable for eigenvalue analysis, frequency extraction, and control design.

S2. REAL-TIME TREMOR MODELING USING RECURSIVE UPDATES

Given the time-varying nature of tremor, real-time updates to the model parameters can improve prediction accuracy [7]. To enable this, we implement a recursive least squares (RLS) algorithm to update the Koopman operator incrementally as new data arrives, following established approaches in [8]–[10].

Let (x_k, u_k) denote the state and input at discrete time k , and let $\Psi_k \in \mathbb{R}^{N_K}$ be the lifted state obtained by applying the observable mapping $\Psi(\cdot)$ to (x_k, u_k) . The matrices $X_{\text{lift}} = [\Psi_1, \dots, \Psi_M] \in \mathbb{R}^{N_K \times M}$ and $X_{\text{lift}}^+ = [\Psi_1^+, \dots, \Psi_M^+] \in \mathbb{R}^{N_K \times M}$ contain M snapshots of the lifted state and its forward-shifted counterpart, respectively, where $\Psi_k^+ = \Psi(x_k^+, u_k^+)$.

In the batch setting, the Koopman operator $K \in \mathbb{R}^{N_K \times N_K}$ is obtained from the normal equation:

$$K = X_{\text{lift}}^+ X_{\text{lift}}^\top (X_{\text{lift}} X_{\text{lift}}^\top)^\dagger, \quad (11)$$

where $(\cdot)^\dagger$ denotes the Moore–Penrose pseudoinverse.

When a new data pair (x_{M+1}, u_{M+1}) and (x_{M+1}^+, u_{M+1}^+) is collected, we can append it to the lifted state matrices:

$$\begin{aligned} X_{\text{lift}_{M+1}} &= [X_{\text{lift}_M}, \Psi_{M+1}], \\ X_{\text{lift}_{M+1}}^+ &= [X_{\text{lift}_M}^+, \Psi_{M+1}^+]. \end{aligned} \quad (12)$$

Here, $\Psi_{M+1} = \Psi(x_{M+1}, u_{M+1})$ and $\Psi_{M+1}^+ = \Psi(x_{M+1}^+, u_{M+1}^+)$.

Directly recomputing (11) after each new sample is computationally expensive. Instead, we define:

$$Q_M = X_{\text{lift}_M}^+ X_{\text{lift}_M}^\top, \quad P_M = (X_{\text{lift}_M} X_{\text{lift}_M}^\top)^\dagger, \quad (13)$$

so that $K_M = Q_M P_M$. Applying the matrix inversion lemma [11], the updated P_{M+1} is:

$$P_{M+1} = P_M - \gamma_{M+1} P_M \Psi_{M+1} \Psi_{M+1}^T P_M, \quad (14)$$

where

$$\gamma_{M+1} = \frac{1}{1 + \Psi_{M+1}^T P_M \Psi_{M+1}}. \quad (15)$$

The Koopman operator update is then:

$$K_{M+1} = K_M + \gamma_{M+1} (\Psi_{M+1}^+ - K_M \Psi_{M+1}) \Psi_{M+1}^T P_M. \quad (16)$$

To emphasize recent data, a forgetting factor $0 < \lambda \leq 1$ can be included in the cost function:

$$\min_{\tilde{K}} \sum_{k=1}^M \lambda^{M-k} \|\Psi_{k+1} - \tilde{K} \Psi_k\|_2^2. \quad (17)$$

Here, \tilde{P}_M denotes the inverse covariance matrix before applying the forgetting factor, and $\hat{P}_M = \tilde{P}_M / \lambda$ is the scaled version used in the weighted update. The corresponding RLS update becomes:

$$\begin{aligned} \tilde{\gamma}_{M+1} &= \frac{1}{1 + \Psi_{M+1}^T \hat{P}_M \Psi_{M+1}}, \\ K_{M+1} &= K_M + \tilde{\gamma}_{M+1} (\Psi_{M+1}^+ - K_M \Psi_{M+1}) \Psi_{M+1}^T \hat{P}_M. \end{aligned} \quad (18)$$

The lifted vectors are $\Psi_k = \Psi(x_k^{\text{IMU}}, u_k^{\text{US}})$ and $\Psi_k^+ = \Psi(x_{k+1}^{\text{IMU}}, u_{k+1}^{\text{US}})$, so the IMU-derived angles are used as the true state and next-state values in the RLS cost (the supervised targets), while ultrasound features are the only exogenous inputs guiding the prediction.

For computational efficiency, we employ a selective update mechanism: let $\bar{X}_M^T = [x_{M-h}, \dots, x_M]$ be the most recent h states, and \hat{X}_M^T the corresponding h -step predictions using K_M . The model is updated only if:

$$\|\bar{X}_M^T - \hat{X}_M^T\|_2^2 \geq \varepsilon, \quad (19)$$

where ε is a user-defined error threshold. This ensures that only information-rich samples trigger an update, maintaining both accuracy and computational efficiency [2].

S3. MUSCLE TISSUE DISPLACEMENT MEASUREMENT USING ULTRASOUND SPECKLE TRACKING

Speckle tracking detects local displacements by computing a normalized cross-correlation function between consecutive ultrasound images:

$$\begin{aligned} \phi(p, q) &= \frac{\sum_{L_{a,b}} (g_{m-1}(a, b) - \bar{g}_{m-1})(g_m(a+p, b+q) - \bar{g}_{m,p,q})}{\sqrt{\sum_{L_{a,b}} (g_{m-1}(a, b) - \bar{g}_{m-1})^2} \times \sqrt{\sum_{L_{a,b}} (g_m(a+p, b+q) - \bar{g}_{m,p,q})^2}}. \end{aligned} \quad (20)$$

where g_{m-1} and g_m represent the image intensities of consecutive frames, and \bar{g}_{m-1} and $\bar{g}_{m,p,q}$ are their respective local averages.

The relative displacement between consecutive frames is then determined as:

$$\Delta_{m,n}(x, y) = \arg \max_{p,q} \{\phi(p, q)\}. \quad (21)$$

To minimize noise, a spatial median filter is applied, refining axial displacement (d_a) and lateral displacement (d_l):

$$d_a = M(\Delta_{x,y}), \quad d_l = M(\Delta_{x,y}), \quad (22)$$

where M denotes the median displacement value. The total tissue displacement (Td) is computed as:

$$Td = \text{sgn}(d_l) \times \sqrt{d_l^2 + d_a^2}. \quad (23)$$

where $\text{sgn}(d_l)$ indicates the direction of lateral motion. The sign of the lateral displacement, $\text{sgn}(d_l)$, is retained in Td so that the total displacement preserves the established directional convention from speckle-tracking literature, where a positive d_l denotes motion to the right and a negative d_l denotes motion to the left [12]. As lateral motion typically represents the dominant component of tremor-related displacement, this convention enables Td to encode both magnitude and primary motion direction in a single scalar, which is advantageous for subsequent analyses such as phase comparison between antagonist muscles.

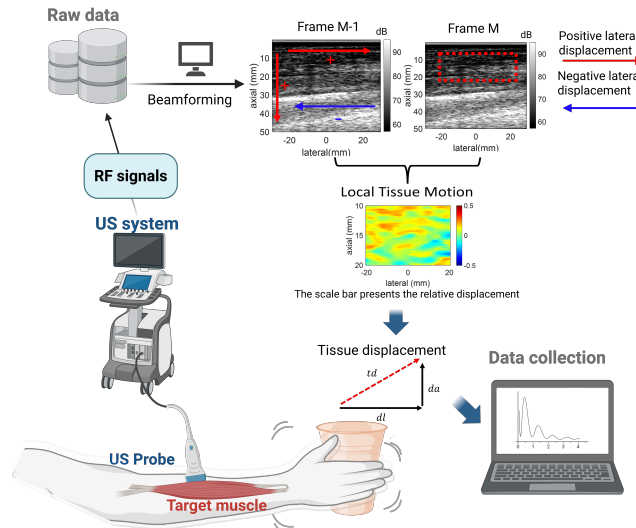


Fig. 1: Workflow for muscle tissue displacement calculation in tremor patients using ultrasound imaging. Legend indicates the positive (rightward) and negative (leftward) lateral displacement directions.

The process for calculating tissue displacement using ultrasound imaging involves several steps, as outlined in Figure 1. This processing step bridges the qualitative visualization capability of ultrasound with quantitative, model-ready features by converting deep muscle motion observed in B-mode images into precise displacement measurements that serve as inputs to the state-space tremor model.

S4. DETAILED CONSTRUCTION OF THE OBSERVABLE FUNCTION FOR EXTENDED DYNAMIC MODE DECOMPOSITION (EDMD)

Our data-driven approach employs Extended Dynamic Mode Decomposition (EDMD) to capture the key dynamics that govern tremor behavior [13] [14]. The EDMD framework represents the system using a lifted state-space model, where the observable function, Ψ_k , transforms the original system states into a higher-dimensional feature space, enabling a more accurate approximation of the system's nonlinear dynamics.

The observable function Ψ_k augments the original state with derivative, harmonic, radial basis, and interaction terms to capture nonlinear tremor dynamics. Specifically, we define

$$\Psi(x_k) = \begin{bmatrix} x_k, \dot{x}_k, \ddot{x}_k \\ \sin(x_k), \cos(x_k), \\ \sin(2x_k), \cos(2x_k), \sin(3x_k), \cos(3x_k) \\ \phi_1(x_k), \phi_2(x_k), \dots, \phi_{N_{RBF}}(x_k) \\ x_{1,k}x_{2,k}, x_{2,k}x_{3,k}, x_{1,k}x_{3,k} \end{bmatrix}, \quad (24)$$

where \dot{x}_k and \ddot{x}_k are first- and second-order finite differences of x_k , and $\phi_j(\cdot)$ are radial basis functions centered at cluster centers obtained via K-means applied to state-space trajectories. The harmonic terms capture oscillatory dynamics characteristic of tremor, while the pairwise interactions provide cross-state coupling features.

The observable function was iteratively evaluated during model training to optimally capture tremor dynamics. The best-performing model configuration was selected based on the simulation with the lowest RMSE among 20 independent runs.

S5. QUANTITATIVE EVALUATION OF DATA-DRIVEN TREMOR DYNAMICS

As tremor dynamics characterize tremor severity, we use derived metrics to validate our data-driven models in the time and frequency domains.

1) Time Domain Analysis: Normalized Root Mean Square Error (NRMSE): We performed a time domain analysis by calculating the Normalized Root Mean Square Error (NRMSE) to quantify the deviations between the original data and the data-driven model output:

$$\text{NRMSE} = \sqrt{\frac{1}{N} \sum_{i=1}^N \left(\frac{y_{\text{actual},i} - y_{\text{predicted},i}}{y_{\text{max}} - y_{\text{min}}} \right)^2}, \quad (25)$$

where $y_{\text{actual},i}$ represents the observed data points, $y_{\text{predicted},i}$ represents the corresponding model predictions, y_{max} and y_{min} are the maximum and minimum values of the observed data, N is the total number of data points, and i is the number of states.

2) Frequency Domain Analysis: Dominant Frequency: The Dominant Frequency refers to the frequency at which the tremor's power is highest. This metric is calculated by identifying the frequency f that maximizes the magnitude of the Fourier Transform $X(f)$:

$$f_{\text{dominant}} = \arg \max_f |X(f)|, \quad (26)$$

where $X(f)$ represents the Fourier Transform of the tremor signal at frequency f . Dominant frequency analysis is essential for characterizing tremor oscillations as it indicates the most prominent frequency within the tremor signal. This metric provides insight into the type and severity of the tremor, which highlights its diagnostic importance [15].

3) Frequency Domain Analysis: Tremor Power Ratio: The Tremor Power Ratio evaluates the proportion of tremor-related spectral power within the 4–12 Hz band, which corresponds to the canonical frequency range of pathological tremors such as essential tremor (ET) and Parkinsonian tremor [16], [17]. The denominator is defined over 0–20 Hz because voluntary movements primarily occur below 3 Hz, while virtually all pathological tremors are confined to the 4–12 Hz range and, more broadly, below 20 Hz [18]. Prior studies also apply a 20 Hz cutoff to exclude higher-frequency noise and to ensure that tremor-related dynamics are well characterized within this bandwidth [19], [20]. It is calculated as follows:

$$\text{Tremor Power Ratio} = \frac{\int_4^{12} |X(f)|^2 df}{\int_0^{20} |X(f)|^2 df}, \quad (27)$$

where $|X(f)|^2$ denotes the power spectral density at frequency f . These integrals are evaluated numerically using discrete summations over the FFT frequency bins. This ratio is particularly useful for isolating tremor-related activity and has been shown to correlate with tremor severity by emphasizing tremor frequencies over other movements [21].

S6. TREMOR EVENT DETECTION AND VALIDATION

A. Tremor Detection Validation

To assess the reliability of tremor detection from the data-driven model, its results are compared to the ground truth detection outcomes. The detected tremor event time steps (T_{true} for the ground truth signals and T_{DD} for the data-driven model) are used to compute performance metrics:

$$\text{TP} = T_{\text{true}} \cap T_{\text{DD}}, \quad (28)$$

$$\text{FP} = T_{\text{DD}} \setminus T_{\text{true}}, \quad (29)$$

$$\text{FN} = T_{\text{true}} \setminus T_{\text{DD}}. \quad (30)$$

Using these values, the following evaluation metrics are computed:

$$\text{Precision} = \frac{\text{TP}}{\text{TP} + \text{FP}}, \quad (31)$$

$$\text{Recall} = \frac{\text{TP}}{\text{TP} + \text{FN}}, \quad (32)$$

$$\text{F1-Score} = 2 \cdot \frac{\text{Precision} \cdot \text{Recall}}{\text{Precision} + \text{Recall}}. \quad (33)$$

B. Tremor Detection Performance

Figure 2 illustrates a representative comparison of tremor detection results obtained from original signals and the data-driven model's predicted signals.

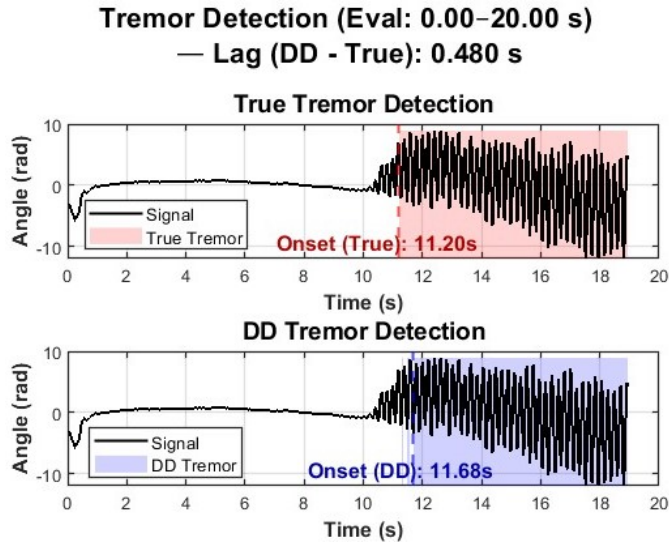


Fig. 2: Comparison of tremor detection results for original IMU signals (top) and the data-driven (DD) model predictions (bottom). Time intervals classified as tremor events are highlighted in red (IMU) and blue (DD). Vertical dashed lines indicate the detected onset of tremor, with onset times annotated on each subplot. In this representative trial, the IMU-based detector reports onset at 11.20 s, while the DD detector reports onset at 11.68 s, corresponding to a lag of 0.48 s. This sub-second lag is consistent with the expected latency introduced by the short-time Fourier analysis window (128 samples at 100 Hz, 50% overlap).

S7. COMPARISON OF MODELING PERFORMANCE BETWEEN ET AND PD PARTICIPANTS

Figure 3 summarizes the modeling performance across ET and PD participants for key evaluation metrics. The mean \pm SD of normalized RMSE (wrist xyz) across trials is summarized in Supplementary Table I.

S8. ONLINE UPDATING WITHOUT EXOGENOUS INPUT

In addition to the models presented in the main text, we evaluated an online adaptive predictor that excludes ultrasound inputs and updates only the state transition matrix. This configuration, referred to as **Case 4**, applies the same selective recursive least-squares (RLS) scheme as Case 3 but without an exogenous input channel. The predictor is therefore written as:

$$x_{k+1} = \hat{A}_k x_k, \quad (34)$$

where $x_k \in \mathbb{R}^3$ denotes the three-axis wrist angle state vector and \hat{A}_k is updated recursively under the same error-threshold criterion (ε) used in Case 3. Case 4 thus serves as a no-input comparator to the ultrasound-augmented model.

Results.: Two representative participants were analyzed: T1 (Parkinson's disease, PD) and T3 (Essential Tremor, ET). Two update thresholds were tested: ε_{low} (frequent updates) and $\varepsilon_{\text{high}}$ (sparser updates). The mean \pm SD of normalized RMSE (wrist xyz) across trials is summarized in Supplementary Table I, with trial-level distributions shown in Fig. 4.

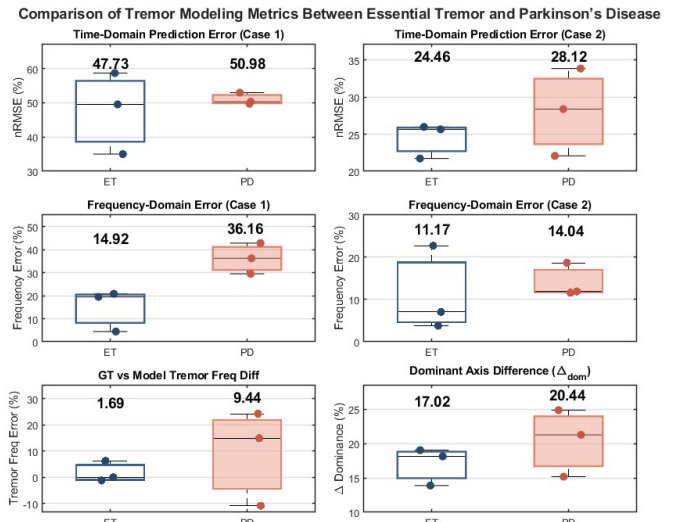


Fig. 3: Group-wise comparison of modeling performance between ET and PD participants across multiple evaluation metrics. Each subplot presents a box-and-scatter plot of performance values for ET (blue) and PD (red) groups.

TABLE I: Mean \pm SD of trial nRMSE for Case 3 (US inputs, selective RLS) and Case 4 (no-input selective RLS).

Participant	Case 3	ε_{low}	Case 3	$\varepsilon_{\text{high}}$
		Case 4		Case 4
T1 (PD)	0.68 ± 0.14	0.69 ± 0.14	20.4 ± 5.3	46.9 ± 57.8
T3 (ET)	0.36 ± 0.11	0.37 ± 0.13	20.6 ± 3.9	27.1 ± 4.2

When updates were frequent, Case 4 achieved accuracy comparable to Case 3. Under sparse updates, however, Case 4 exhibited degraded performance, whereas Case 3 maintained lower mean error and reduced variability (Supplementary Table I; Fig. 4).

Interpretation.: Several factors likely explain why ultrasound inputs stabilize performance when updates are sparse. (i) *Persistent excitation*. Recursive identification requires informative regressor variation to adapt reliably. For $x_{k+1} = \hat{A}_k x_k + \hat{B}_k u_k$, the RLS gain depends on $S_M = \sum_k \phi_k \phi_k^\top$ with $\phi_k = [x_k^\top \ u_k^\top]^\top$. When no input is present, or when x_k varies weakly/collinearly, S_M becomes ill-conditioned, leading to slow adaptation and compounded bias between updates. (ii) *Bias and drift propagation*. IMU-derived angles can accumulate low-frequency bias and drift due to temporal integration. In a no-input model, this bias is propagated directly by \hat{A}_k , so small offsets accumulate over open-loop intervals between updates. (iii) *Ultrasound excitation*. Ultrasound features encode localized muscle-level oscillations in the tremor band that are not redundant with x_k . This independent excitation improves the conditioning of S_M , enhances observability of oscillatory modes, and yields informative RLS corrections even under sparse updates.

S9. EXTENDED INTERPRETATION OF ET–PD TRENDS

Our modeling results demonstrated consistently higher predictive accuracy for ET cases compared to PD across both time

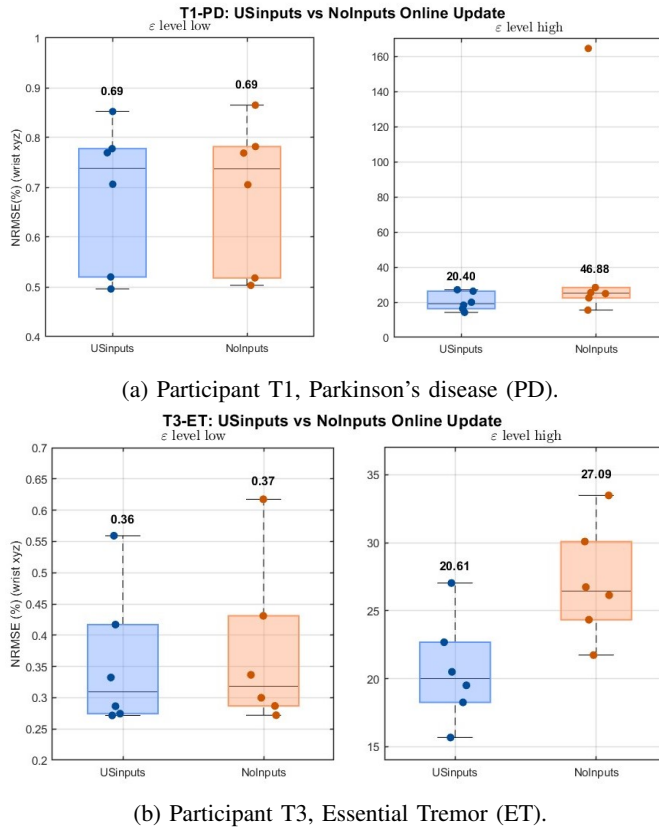


Fig. 4: Comparison of Case 3 (US input with selective RLS updates) versus Case 4 (no-input selective RLS) under two error thresholds ε . Left: ε_{low} ; Right: $\varepsilon_{\text{high}}$. Annotated medians show three-axis nRMSE for each trial. Summary statistics are reported in Supplementary Table I.

and frequency domains. This trend reflects well-established physiological distinctions between the two conditions [16], [17]. Essential tremor is typically expressed during voluntary movement or sustained posture, both of which were intentionally elicited by the grasp-and-hold task used in this study. In contrast, Parkinsonian tremor is most prominently observed at rest, often diminishes during the initiation of voluntary movement, and may reappear during sustained postures with variable onset timing. This variability likely introduced greater inter- and intra-trial inconsistency in PD participants, making it more difficult for the data-driven models to extract stable dynamic patterns.

The consistently lower modeling error in ET participants may be attributed to the generally more continuous and rhythmic nature of essential tremor during voluntary tasks, which provides richer and more stable temporal patterns for the learning algorithm [22], [23]. In contrast, Parkinsonian tremor tends to occur intermittently and is often suppressed during movement, with re-emergence during sustained postures only after variable latency, leading to greater variability across trials [24], [25]. This irregularity likely introduced periods of signal quiescence or mixed activity in PD data, making it more challenging for the model to learn consistent tremor dynamics. Although the frequency-domain improvement from Case 1

to Case 2 was greater in PD than in ET, this is consistent with the higher baseline error in PD rather than indicating a stronger benefit from ultrasound input. Overall, the modeling framework demonstrated higher accuracy in ET across all absolute error metrics.

These quantitative trends are consistent with the observed frequency-domain agreement metrics: ET participants exhibited near-perfect correlation with ground truth ($R^2 = 0.964$, nRMSE=2.0%), whereas PD participants showed weaker correlation ($R^2 = 0.333$, nRMSE=17.5%). This disparity directly reflects the greater trial-to-trial variability of Parkinsonian tremor. Importantly, despite reduced statistical agreement, the model still preserved physiologically relevant oscillatory content in PD, indicating usability across tremor phenotypes.

Importantly, the tremor frequencies identified by the model were consistent with expected clinical ranges for both groups. Model-estimated frequencies for PD participants fell within the 4–6 Hz range commonly associated with resting tremor, while those for ET participants were within the broader 4–12 Hz range typical of postural and action tremors. This alignment supports the physiological validity of the model's frequency decomposition and suggests that the approach preserved key spectral features of each tremor subtype.

While the present analysis focused on ET and PD participants performing a grasp-and-hold task, the framework's applicability to other tremor types (e.g., dystonic, orthostatic) and across different movement states (resting, postural, and kinetic) remains to be systematically investigated. The current findings suggest that rhythmic and continuous tremor patterns, such as those in ET, are more amenable to stable modeling, whereas the intermittent expression of PD tremor poses greater challenges. Future studies with larger and more diverse cohorts will be necessary to assess how tremor severity, phenotype, and task context influence model accuracy and to validate whether the observed ET–PD disparity generalizes across broader patient populations. Beyond global metrics such as frequency and amplitude, the eigenvalue-based analysis provides a structured way to link model-derived features to clinically interpretable parameters. The dominant state contributions $\Delta_{\text{dominance}}$ quantify how strongly each anatomical axis participates in tremor generation, directly reflecting the relative involvement of the agonist–antagonist muscle groups responsible for that degree of freedom. This axis-specific information may support therapy targeting; for example, informing orthotic damping strategies or optimizing stimulation placement for the most affected DOF. Moreover, the temporal evolution of eigenmodes offers a quantitative approach to characterize changes in tremor severity or stability over time, and may serve as a potential biomarker for monitoring disease progression or treatment response. Collectively, these features provide physiologically grounded parameters that can complement established clinical scales such as TETRAS or MDS-UPDRS in both diagnostic and interventional contexts, and future studies will aim to directly correlate these features with clinical rating scales to enhance their generalizability as outcome measures.

S10. IMPLEMENTATION AND TRANSLATION NOTES

The development of this ultrasound-enhanced data-driven tremor model serves as a crucial step toward real-world applications, particularly in tremor suppression and event detection. Because both detectors are window-based, they exhibit a sub-second latency (~ 0.5 s in this study). Future work may reduce this lag by using shorter windows, smaller hops, or causal onset detection rules, which would further improve real-time responsiveness.

The linear structure of the model facilitates the application of control theory for tremor suppression strategies. By transforming tremor dynamics into a structured state-space framework, the model enables the design of model-based controllers, such as Model Predictive Control (MPC), to optimize afferent stimulation parameters for tremor mitigation. The ability to predict tremor states in real-time allows for closed-loop control, where stimulation can be adaptively modulated based on model predictions, enhancing the effectiveness of suppression interventions.

The superior performance of Case 2 suggests a practical calibration strategy for sensor reduction. In the training stage, both wrist motion data and US inputs can be collected as reference signals. Once the model is trained, wrist angle sensors could be removed, and US data alone could be used for tremor prediction. This would enable a more compact and wearable system, reducing reliance on motion capture devices while maintaining reliable tremor tracking.

From a clinical perspective, this framework can complement existing diagnostic and monitoring practices by providing objective, quantitative measures of tremor frequency and amplitude. Continuous ultrasound-based monitoring could support tracking of disease progression and treatment response, while the model's predictive capability offers a foundation for adaptive, patient-specific stimulation protocols in real-world clinical settings.

S11. EXTENDED LIMITATIONS AND FUTURE WORK

While the present study demonstrates the feasibility and advantages of integrating ultrasound-derived features into a data-driven tremor model, several limitations should be acknowledged. First, the ultrasound sensing in this work targeted either the FCR or ECR in each trial. These antagonist muscle groups are primary contributors to wrist flexion–extension along the anatomical y -axis, which is a dominant component of tremor-related motion. Consequently, the ultrasound-derived tissue displacement measurements represent two-dimensional motion in the axial and lateral imaging planes rather than the full three-dimensional tremor kinematics. To capture tremor across all three anatomical axes (x , y , and z), additional imaging sites would be required, such as the flexor carpi ulnaris (FCU) and extensor carpi ulnaris (ECU) for x -axis motion, and pronator–supinator muscle groups for z -axis motion. This multi-site configuration was beyond the scope of the present study but represents a natural direction for future work. Moreover, the current probe configuration inherently limits displacement tracking to axial and lateral components because

conventional B-mode imaging does not acquire elevational displacement.

Another limitation is the relatively small sample size ($n = 6$), with equal representation from ET and PD participants. This restricts the generalizability of the reported group-wise trends. Future studies should incorporate larger and more diverse cohorts, including different tremor phenotypes and severity levels, to validate model robustness and to assess whether the observed performance differences persist across populations. Nonetheless, the consistent differences observed between ET and PD participants in this study align with well-established physiological distinctions between the two tremor types despite the limited cohort size. The small sample size precluded stratified subgroup analyses across these factors. Future studies with larger, more diverse cohorts will allow evaluation of how age, tremor severity, and hand dominance influence model accuracy and generalization.

In addition, the present segmentation strategy, training on the first half of each trial and testing on the second half, may lead to optimistic estimates of generalization, since both partitions originate from the same trial. Future work will therefore implement trial-level or subject-level hold-out schemes to better assess model robustness and reduce the risk of overfitting.

Relatedly, although Case 3 was described as an “online update” model, its implementation in this study was performed offline for post hoc analysis. While the recursive least squares (RLS) formulation is explicitly designed for streaming data and is computationally lightweight, sensor shifts, changes in probe–skin coupling, and movement artifacts may introduce additional variability during real-time deployment. Future work will therefore implement Case 3 in a streaming pipeline with wearable ultrasound hardware to evaluate robustness under naturalistic conditions.

A further limitation is that the present framework integrates ultrasound and IMU data in a structured but relatively simple manner, without explicitly modeling cross-modal correlations. Prior work from our group has shown that ultrasound- and IMU-derived tremor metrics are highly correlated in the 4–12 Hz band, while ultrasound remains robust to stimulation artifacts [12]. Building on these findings, future work will explore advanced fusion approaches (e.g., canonical correlation analysis or multimodal learning) to more fully exploit the complementary information across sensing modalities.

Finally, extending ultrasound sensing to a multi-site arrangement could enable full 3D tremor characterization and potentially enhance predictive accuracy. This expanded sensing strategy is expected to improve performance in scenarios such as those observed in Case 2, where single-axis measurements may have underrepresented the complete tremor motion. A further methodological extension concerns the system’s observability. In the current framework the wrist angles are directly defined as the model states, making the system trivially observable. Ultrasound features are treated as exogenous inputs, which improves conditioning and predictive accuracy but does not alter the formal observability structure. Future work could instead augment the state vector with muscle-level ultrasound features, enabling a formal observability analysis

and clarifying how ultrasound improves state estimation in a theoretical sense. Such an approach, combined with larger-scale clinical validation, would provide a stronger foundation for translating this modeling framework into practical, wearable tremor monitoring and suppression systems.

REFERENCES

- [1] B. O. Koopman, "Hamiltonian systems and transformation in hilbert space," *Proceedings of the national academy of sciences of the united states of america*, vol. 17, no. 5, p. 315, 1931.
- [2] X. Xue, A. Iyer, and N. Sharma, "Koopman-based data-driven model predictive control of limb tremor dynamics with online model updating: A theoretical modeling and simulation approach," in *2023 American Control Conference (ACC)*, pp. 2873–2878, IEEE, 2023.
- [3] M. Korda and I. Mezić, "Linear predictors for nonlinear dynamical systems: Koopman operator meets model predictive control," *Automatica*, vol. 93, pp. 149–160, 2018.
- [4] E. Kaiser, J. N. Kutz, and S. L. Brunton, "Data-driven approximations of dynamical systems operators for control," in *The Koopman Operator in Systems and Control*, pp. 197–234, Springer, 2020.
- [5] S. Klus, F. Nüske, S. Peitz, J.-H. Niemann, C. Clementi, and C. Schütte, "Data-driven approximation of the koopman generator: Model reduction, system identification, and control," *Physica D: Nonlinear Phenomena*, vol. 406, p. 132416, 2020.
- [6] J. L. Proctor, S. L. Brunton, and J. N. Kutz, "Generalizing koopman theory to allow for inputs and control," *SIAM Journal on Applied Dynamical Systems*, vol. 17, no. 1, pp. 909–930, 2018.
- [7] F. M. Hemez and S. W. Doebling, "Review and assessment of model updating for non-linear, transient dynamics," *Mechanical Systems and Signal Processing*, vol. 15, no. 1, pp. 45–74, 2001.
- [8] T. C. Hsia, *System identification: least-squares methods*. Free Press, 1977.
- [9] H. M. Calderón, E. Schulz, T. Oehlschlägel, and H. Werner, "Koopman operator-based model predictive control with recursive online update," in *2021 European Control Conference (ECC)*, pp. 1543–1549, IEEE, 2021.
- [10] H. Zhang, C. W. Rowley, E. A. Deem, and L. N. Cattafesta, "Online dynamic mode decomposition for time-varying systems," *SIAM Journal on Applied Dynamical Systems*, vol. 18, no. 3, pp. 1586–1609, 2019.
- [11] K. J. Åström and B. Wittenmark, *Adaptive control*. Courier Corporation, 2013.
- [12] A. Iyer, X. Xue, V. Ganesh, X. Jiang, C. Gallippi, D. Roque, and N. Sharma, "Ultrasound imaging triggered tremor suppression with personalized afferent stimulation frequency," *IEEE Transactions on Biomedical Engineering*, 2024.
- [13] S. L. Brunton and J. N. Kutz, *Data-driven science and engineering: Machine learning, dynamical systems, and control*. Cambridge University Press, 2022.
- [14] M. O. Williams, I. G. Kevrekidis, and C. W. Rowley, "A data-driven approximation of the koopman operator: Extending dynamic mode decomposition," *Journal of Nonlinear Science*, vol. 25, no. 6, pp. 1307–1346, 2015.
- [15] J. Timmer, "Modeling noisy time series: physiological tremor," *International Journal of Bifurcation and Chaos*, vol. 8, no. 07, pp. 1505–1516, 1998.
- [16] M.-K. Pan, "Targeting the fundamentals for tremors: the frequency and amplitude coding in essential tremor," *Journal of biomedical science*, vol. 32, no. 1, p. 18, 2025.
- [17] A. H. Abusrair, W. Elsekaily, and S. Bohlega, "Tremor in parkinson's disease: from pathophysiology to advanced therapies," *Tremor and Other Hyperkinetic Movements*, vol. 12, p. 29, 2022.
- [18] G. Deuschl, J. Raethjen, M. Lindemann, and P. Krack, "The pathophysiology of tremor," *Muscle & Nerve: Official Journal of the American Association of Electodiagnostic Medicine*, vol. 24, no. 6, pp. 716–735, 2001.
- [19] D. Zhang, X. Zhu, and P. Poignet, "Coupling of central and peripheral mechanism on tremor," in *2009 4th International IEEE/EMBS Conference on Neural Engineering*, pp. 649–652, IEEE, 2009.
- [20] A. Medvedev, F. Olsson, and T. Wigren, "Tremor quantification through data-driven nonlinear system modeling," in *2017 IEEE 56th Annual Conference on Decision and Control (CDC)*, pp. 5943–5948, IEEE, 2017.
- [21] R. J. Elble, "Gravitational artifact in accelerometric measurements of tremor," *Clinical Neurophysiology*, vol. 116, no. 7, pp. 1638–1643, 2005.
- [22] D. Haubenberger and M. Hallett, "Essential tremor," *New England Journal of Medicine*, vol. 378, no. 19, pp. 1802–1810, 2018.
- [23] Z. Farkas, A. Csillik, L. Pálvölgyi, A. Takács, I. Szirmai, and A. Kamondi, "Complex tremor analysis for the differential diagnosis of essential tremor and parkinson's disease," *Ideggogyógyászati szemle*, vol. 59, no. 1-2, pp. 45–54, 2006.
- [24] W. Chen, F. Hopfner, J. S. Beckepe, and G. Deuschl, "Rest tremor revisited: Parkinson's disease and other disorders," *Translational neurodegeneration*, vol. 6, no. 1, p. 16, 2017.
- [25] P. Kugler, C. Jaremenko, J. Schlachetzki, J. Winkler, J. Klucken, and B. Eskofier, "Automatic recognition of parkinson's disease using surface electromyography during standardized gait tests," in *2013 35th Annual International Conference of the IEEE Engineering in Medicine and Biology Society (EMBC)*, pp. 5781–5784, IEEE, 2013.